

Suppressing the intestinal farnesoid X receptor/sphingomyelin phosphodiesterase 3 axis decreases atherosclerosis

Qing Wu,^{1,2,3} Lulu Sun,⁴ Xiaomin Hu,⁵ Xuemei Wang,^{1,2,3} Feng Xu,^{1,2,3} Bo Chen,^{1,2,3} Xianyi Liang,^{1,2,3} Jialin Xia,^{1,2,3} Pengcheng Wang,^{1,2,3} Daisuke Aibara,⁴ Shaofei Zhang,⁴ Guangyi Zeng,^{1,2,3} Chuyu Yun,^{1,2,3} Yu Yan,^{1,2,3} Yicheng Zhu,⁵ Michael Bustin,⁴ Shuyang Zhang,⁵ Frank J. Gonzalez,⁴ and Changtao Jiang^{1,2,3}

¹Department of Physiology and Pathophysiology, School of Basic Medical Sciences, Peking University, and the Key Laboratory of Molecular Cardiovascular Science, Ministry of Education, Beijing, China.

²Center of Basic Medical Research, Institute of Medical Innovation and Research, Third Hospital, Peking University, Beijing, China. ³Center for Obesity and Metabolic Disease Research, School of Basic Medical Sciences, Peking University, Beijing, China. ⁴Laboratory of Metabolism, Center for Cancer Research, National Cancer Institute, NIH, Bethesda, Maryland, USA. ⁵Peking Union Medical College Hospital, Chinese Academy of Medical Sciences & Peking Union Medical College, Beijing, China.

Intestinal farnesoid X receptor (FXR) signaling is involved in the development of obesity, fatty liver disease, and type 2 diabetes. However, the role of intestinal FXR in atherosclerosis and its potential as a target for clinical treatment have not been explored. The serum levels of fibroblast growth factor 19 (FGF19), which is encoded by an FXR target gene, were much higher in patients with hypercholesterolemia than in control subjects and were positively related to circulating ceramide levels, indicating a link between intestinal FXR, ceramide metabolism, and atherosclerosis. Among *ApoE*^{-/-} mice fed a high-cholesterol diet (HCD), intestinal FXR deficiency (in *Fxr*^{ΔE} *ApoE*^{-/-} mice) or direct FXR inhibition (via treatment with the FXR antagonist glyoursodeoxycholic acid [GUDCA]) decreased atherosclerosis and reduced the levels of circulating ceramides and cholesterol. Sphingomyelin phosphodiesterase 3 (SMPD3), which is involved in ceramide synthesis in the intestine, was identified as an FXR target gene. SMPD3 overexpression or C16:0 ceramide supplementation eliminated the improvements in atherosclerosis in *Fxr*^{ΔE} *ApoE*^{-/-} mice. Administration of GUDCA or GW4869, an SMPD3 inhibitor, elicited therapeutic effects on established atherosclerosis in *ApoE*^{-/-} mice by decreasing circulating ceramide levels. This study identified an intestinal FXR/SMPD3 axis that is a potential target for atherosclerosis therapy.

Introduction

Atherosclerosis is a chronic disease featuring hypercholesterolemia and chronic inflammation (1). Farnesoid X receptor (FXR) is a ligand-activated nuclear receptor that regulates cholesterol and bile acid metabolism and has been suggested to be involved in atherosclerosis (2). Previous correlative studies have suggested that whole-body FXR signaling affects the initiation and progression of atherosclerosis in mice, but the results have been inconsistent (3–5). *Fxr*^{-/-} mice display an attenuated atherosclerotic phenotype (3), while treatment of mice with the synthetic FXR agonist obeticholic acid (OCA) lowers serum cholesterol, an effect that is dependent on activation of hepatic FXR (6). These findings indicate that intestinal and hepatic FXR signaling may play different roles in atherosclerosis as well as in obesity-induced metabolic diseases (6).

Hypercholesterolemia is a well-established independent risk factor for atherosclerosis that results in monocytes and accumulation of cholesterol-laden foam cells in the artery walls (7).

Hepatic cholesterol catabolism is the main pathway for cholesterol elimination, which plays an important role in systemic cholesterol homeostasis and the pathogenesis of atherosclerosis (8). In the liver, cholesterol is converted into primary bile acids that are then secreted into the intestine as taurine and glycine conjugates (9). Hepatic CYP7A1 is the rate-limiting enzyme in the classical bile acid synthesis pathway, which accounts for approximately 75% of bile acid production (9). The intestinal FXR/fibroblast growth factor 15/19 (FGF15/19, where FGF15 is the murine protein and FGF19 is the human ortholog) axis is the main suppressor of *Cyp7a1* expression, whereas the hepatic FXR/small heterodimer partner (SHP) pathway shows only minor inhibitory effects (10). Thus, intestinal FXR might regulate cholesterol catabolism through modulating hepatic CYP7A1 activity.

Circulating ceramides are also considered important risk factors for cardiovascular disease (11). Hyperaccumulation of ceramides is thought to induce foam cell formation and promote toxicity to multiple types of cells (e.g., endothelial cells [ECs], cardiomyocytes) and consequently to play roles in the pathogenesis of diabetes, hypertension, heart failure, and atherosclerosis (12–16). Recent clinical trials have revealed that circulating ceramide levels correlate strongly with cardiovascular events, such as myocardial infarction and stroke (17–19). Although ceramides have been identified as biomarkers of cardiovascular disease endpoints

Authorship note: QW, LS, and XH contributed equally to this work.

Conflict of interest: The authors have declared that no conflict of interest exists.

Copyright: © 2021, American Society for Clinical Investigation.

Submitted: August 3, 2020; **Accepted:** March 11, 2021; **Published:** May 3, 2021.

Reference information: *J Clin Invest.* 2021;131(9):e142865.

<https://doi.org/10.1172/JCI142865>.

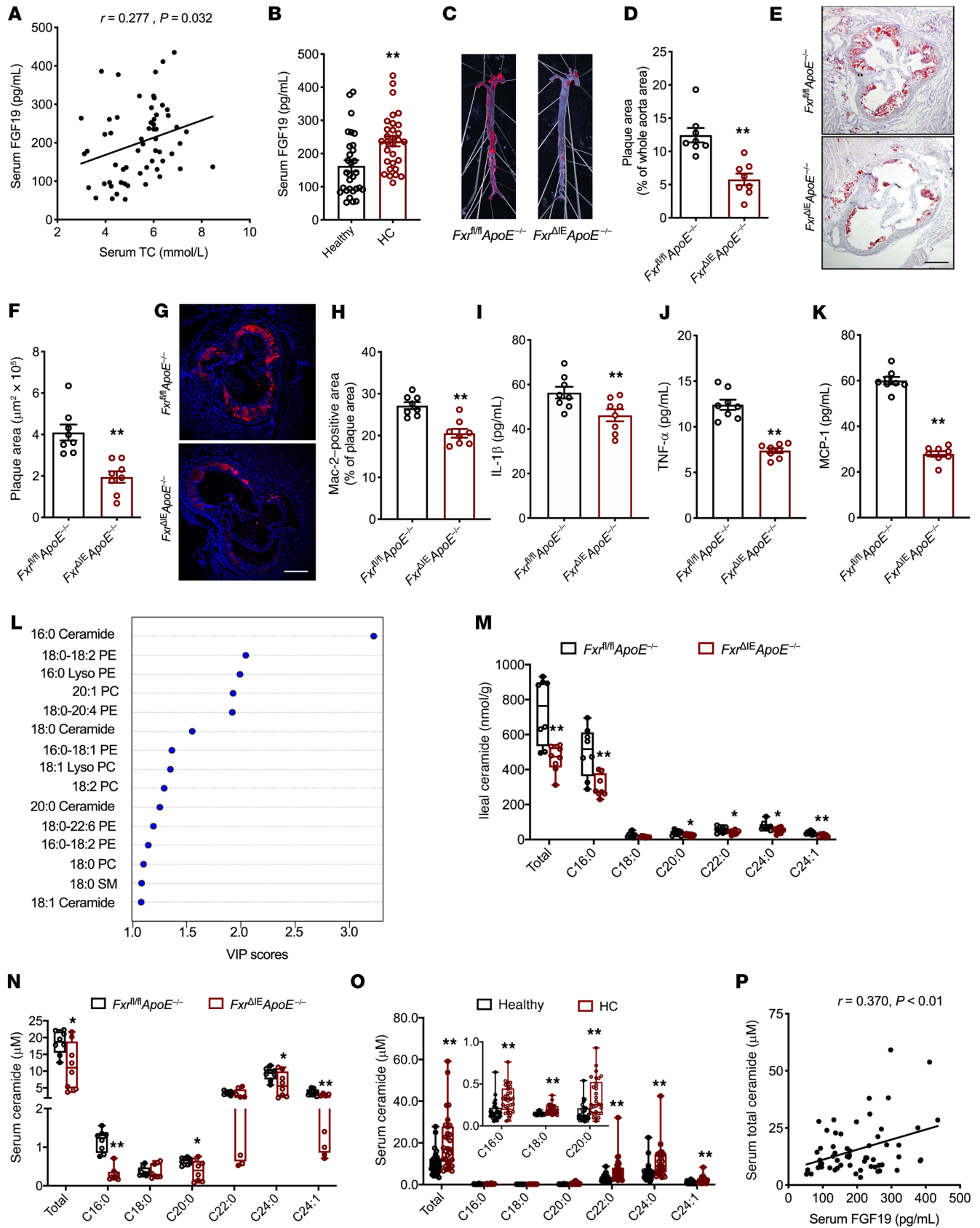


Figure 1. Deficiency of intestinal FXR alleviates atherosclerosis and decreases circulating ceramide levels. Clinical serum samples ($n = 60$) were collected from healthy humans ($n = 30$) and patients with hypercholesterolemia (HC; serum TC > 6.2 mmol/L, $n = 30$). *Fxr^{fl/fl} ApoE^{-/-}* and *Fxr^{ΔIE} ApoE^{-/-}* mice were fed an HCD for 5 weeks ($n = 8$ /group). (A) Pearson's correlation analysis between serum TC and FGF19 levels in humans. (B) Serum FGF19 levels in healthy humans and patients with hypercholesterolemia. (C and D) Representative images of aortas stained with Oil Red O (C) and quantification of the lesions (D). (E and F) Representative sections of the left ventricular outflow tract stained with Oil Red O (E) and the quantified lesion areas (F). (G and H) Representative images of left ventricular outflow tract sections stained for Mac-2 (G) and the calculated Mac-2-positive areas in the plaques (H). (I–K) Levels of the proinflammatory cytokines IL-1 β (I), TNF- α (J), and MCP-1 (K) in the serum. (L) VIP score plot showing the top 15 proinflammatory lipid metabolites in the ileum that led to the separation between *Fxr^{fl/fl} ApoE^{-/-}* and *Fxr^{ΔIE} ApoE^{-/-}* mice ($n = 16$) (shown in Supplemental Figure 2H). PE, phosphatidylethanolamine; PC, phosphatidylcholine; SM, sphingomyelin. (M) Quantification of ileal ceramides. (N) Quantification of serum ceramides in mice. (O) Quantification of serum ceramides in healthy humans and patients with hypercholesterolemia. (P) Pearson's correlation analysis between serum FGF19 and total ceramide levels in humans. The data are presented as the mean \pm SEM. Two-tailed Student's t test: $**P < 0.01$ versus healthy (B) or *Fxr^{fl/fl} ApoE^{-/-}* (D, F, and H–K). Mann-Whitney U test: $*P < 0.05$, $**P < 0.01$ versus *Fxr^{fl/fl} ApoE^{-/-}* (M and N) or healthy (O). Scale bars: 200 μ m.

(20–22), the underlying mechanism of ceramide metabolism imbalance during atherosclerosis progression is unclear. There are 3 major pathways of ceramide generation regulated by various enzymes: the sphingomyelinase, de novo synthesis, and salvage pathways (23). Experimental manipulations of these enzymes in animal models of metabolic diseases have revealed that decreasing ceramide levels by inhibiting synthesis or promoting degradation ameliorates insulin resistance, steatohepatitis, and atherosclerosis (16, 24). Recent studies have also shown that inhibition of intestinal FXR can reduce ceramide levels to improve obesity and diabetes (25, 26). These studies suggest that intestinal FXR is a major regulator of intestinal ceramide production.

In the current study, intestinal FXR was found to be significantly activated in patients with hypercholesterolemia and mice fed a high-cholesterol diet (HCD). Activation of intestinal FXR upregulated sphingomyelin phosphodiesterase 3-mediated (SMPD3-mediated) ceramide production and suppressed CYP7A1-mediated cholesterol catabolism, which potentiated atherosclerosis. Moreover, *Smpd3* was identified as an FXR target gene. Inhibition of the intestinal FXR/SMPD3 axis exerted therapeutic effects on atherosclerosis by decreasing circulating ceramide levels.

Results

Intestine-specific *Fxr* disruption reduces atherosclerosis. To determine the relationship between intestinal FXR signaling and atherosclerosis, human serum samples were analyzed. Serum FGF19 levels were positively related to serum total cholesterol (TC) levels and were elevated in patients with hypercholesterolemia (Figure 1, A and B). Consistent with this finding, the expression of intestinal FXR target genes was markedly upregulated in mice fed an HCD (Supplemental Figure 1A; supplemental material available online with this article; <https://doi.org/10.1172/JCI142865DS1>). These results indicate that intestinal FXR is activated during the progression of atherosclerosis. To explore the role of intestinal FXR

signaling in atherosclerotic progression, intestine-specific FXR and APOE double-knockout (KO) (*Fxr^{ΔIE} ApoE^{-/-}*) mice were generated (Supplemental Figure 1B). To avoid the interfering effects of obesity, we chose a proatherosclerotic diet that did not induce an obvious body weight increase (Supplemental Figure 1C). Under this diet, loss of intestinal FXR had no effects on obesity and insulin resistance (Supplemental Figure 1, C–I). Oil Red O staining revealed that, compared with the HCD-fed *Fxr^{fl/fl} ApoE^{-/-}* mice, the HCD-fed *Fxr^{ΔIE} ApoE^{-/-}* mice exhibited smaller lesions in both the en face aortas and sections of the aortic roots (Figure 1, C–F). Correspondingly, the hepatic and serum cholesterol levels in HCD-fed *Fxr^{ΔIE} ApoE^{-/-}* mice were lower than those in HCD-fed *Fxr^{fl/fl} ApoE^{-/-}* mice (Supplemental Figure 1, J–L). Intestinal cholesterol transport- and hepatic cholesterol synthesis-related gene mRNA levels did not differ between the two groups, but the mRNA levels of the cholesterol transport genes *Ldlr* and *Abcg8* were slightly elevated in the liver (Supplemental Figure 1, M and N). It was reported that FGF15/19 binds to FGF receptor 4 (FGFR4) to suppress hepatic expression of CYP7A1 (10), the key enzyme involved in cholesterol catabolism. As a result of intestinal FXR inhibition and reduced FGF15 production, hepatic *Cyp7a1* mRNA levels were elevated, which was the main contributing factor to the decreases in serum and hepatic cholesterol levels in HCD-fed *Fxr^{ΔIE} ApoE^{-/-}* mice (Supplemental Figure 1O). In humans, serum FGF19 levels were also negatively related to serum levels of 7 α -hydroxycholesterol (C4), the product of CYP7A1-mediated cholesterol metabolism (Supplemental Figure 1P). Serum C4 levels were much lower in patients with hypercholesterolemia than in controls and were negatively related to serum TC levels (Supplemental Figure 1, Q and R). Hepatic CYP7A1-mediated cholesterol catabolism is suppressed as a result of activation of the intestinal FXR/FGF19 axis in patients with hypercholesterolemia. To explore the underlying mechanism of atherosclerosis relief, the relative expression levels of several atherosclerosis-related markers indicating the dysfunction of macrophages, vascular smooth muscle cells (VSMCs), and ECs were analyzed (27–29). mRNA levels of macrophage markers (cluster of differentiation 68, *Cd68* and cluster of differentiation 11c, *Cd11c*) were downregulated, and NLRP3 inflammasome markers (NLR family pyrin domain containing 3, *Nlrp3* and interleukin 1 β , *Il1b*) and the scavenger receptor (cluster of differentiation 36, *Cd36*) were significantly decreased in aortas of *Fxr^{ΔIE} ApoE^{-/-}* mice compared with those of *Fxr^{fl/fl} ApoE^{-/-}* mice (Supplemental Figure 2A). There was no change in the relative expression of VSMC and EC markers (myosin heavy chain 11, *Myh11* and kinase insert domain receptor, *Kdr*), and the mRNA levels of genes involved in VSMC proliferation and migration (proliferating cell nuclear antigen, *Pcna* and matrix metalloproteinase 2, *Mmp2*), indicators of oxidative stress (NADPH oxidase 2, *Nox2* and nitric oxide synthase 3, *Nos3*) and adhesion molecules (intercellular adhesion molecule 1, *Icam1* and vascular cell adhesion protein 1, *Vcam1*) of ECs, which were similar between the two groups (Supplemental Figure 2A). This finding indicated that elevated inflammation and CD36 expression in the vasculature were mainly suppressed in *Fxr^{ΔIE} ApoE^{-/-}* mice. Sections of the aortic roots were stained for Mac-2, revealing that macrophage populations were reduced in the HCD-fed *Fxr^{ΔIE} ApoE^{-/-}* mice (Figure 1, G and H). In plaques of aortic roots, IL-1 β and CD36 expression in macrophages was

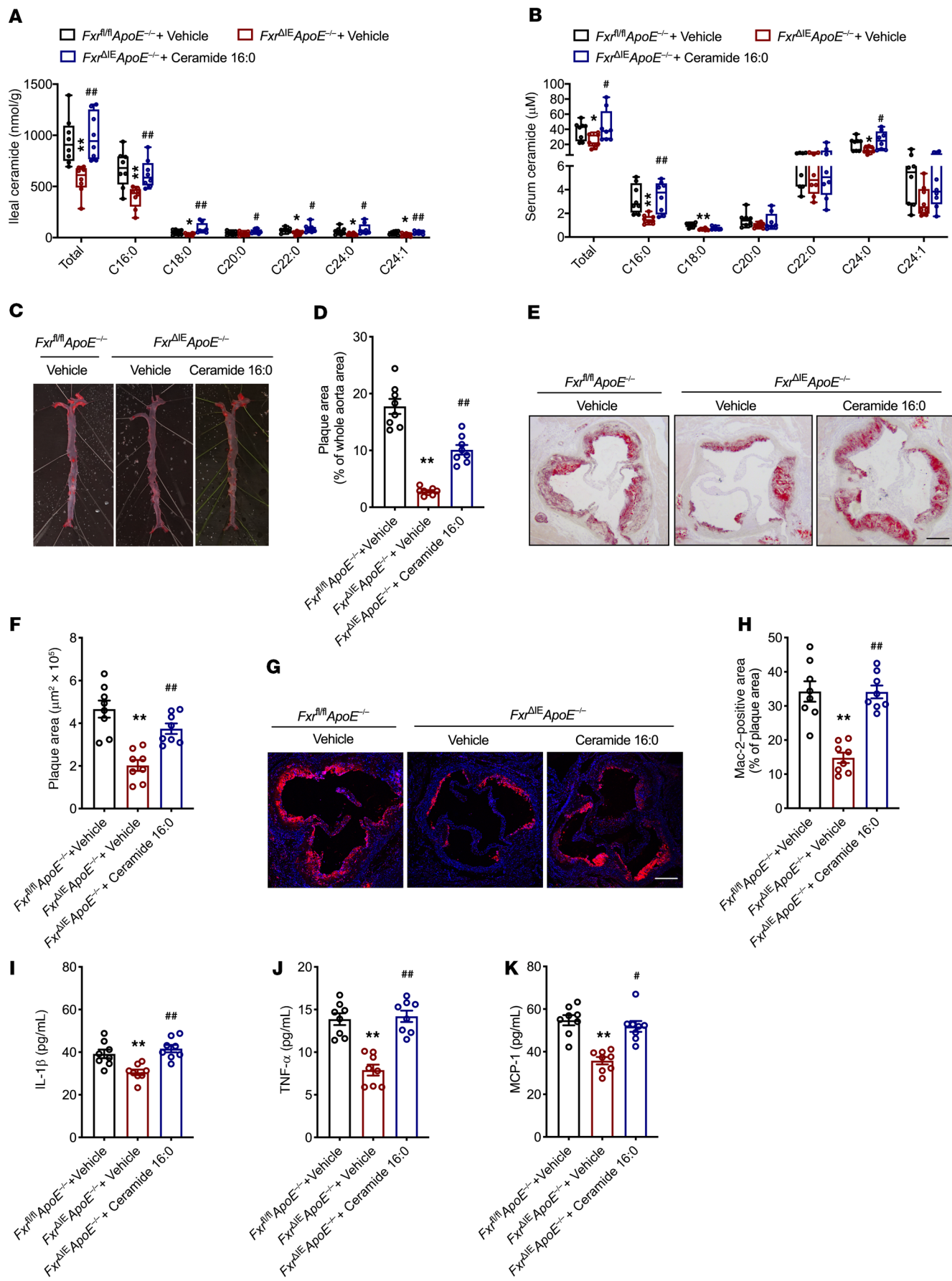


Figure 2. Replenishment of C16:0 ceramide partially reverses improvements in atherosclerosis resulting from loss of intestinal FXR. *Fxr^{fl/fl} ApoE^{-/-}* and *Fxr^{fl/fl} ApoE^{-/-}* mice were treated with vehicle or C16:0 ceramide (10 mg/kg/d) by i.p. injection during HCD feeding for 5 weeks ($n = 8/\text{group}$). (A and B) Levels of ceramides in the ileum (A) and serum (B). (C and D) Representative images of aortas stained with Oil Red O (C) and quantification of the lesions (D). (E and F) Representative sections of left ventricular outflow tracts stained with Oil Red O (E) and the quantified lesion areas (F). (G and H) Immunofluorescence staining of atherosclerotic lesions for Mac-2 (G) and quantification of the positive areas (H). (I–K) Serum levels of the proinflammatory cytokines IL-1 β (I), TNF- α (J), and MCP-1 (K). The data are presented as the mean \pm SEM. Kruskal-Wallis test with Dunn's post hoc test (A and B) and 1-way ANOVA with Tukey's post hoc test (D, F, and H–K): * $P < 0.05$ and ** $P < 0.01$ versus *Fxr^{fl/fl} ApoE^{-/-}* + vehicle and # $P < 0.05$, ## $P < 0.01$ versus *Fxr^{fl/fl} ApoE^{-/-}* + vehicle. Scale bars: 200 μm .

much lower in the absence of intestinal FXR than in the presence of this molecule (Supplemental Figure 2, B–E). Circulating inflammatory cytokine levels were also much lower in HCD-fed *Fxr^{fl/fl} ApoE^{-/-}* mice than in HCD-fed *Fxr^{fl/fl} ApoE^{-/-}* mice (Figure 1, I–K, and Supplemental Figure 2, F and G). These data indicate that intestine-specific ablation of FXR alleviates HCD-induced inflammation and hypercholesterolemia, which likely contributes to the improvement of atherosclerosis in *ApoE^{-/-}* mice.

Reduction of the serum ceramide pool accounts for the improvements in the absence of intestinal FXR. To explore which key factors mediate the beneficial effects of intestinal FXR modulation, proinflammatory lipid profiles were measured. Partial least squares discriminant analysis (PLS-DA) revealed that intestinal lipid profiles differed between the two groups (Supplemental Figure 2H). Among the intestinal lipid species, C16:0 ceramide was the main driver of the separation of intestinal proinflammatory lipids between the two groups (Figure 1L). In *ApoE^{-/-}* mice, ceramide levels in the ileum were much lower in the absence than in the presence of intestinal FXR (Figure 1M). Moreover, loss of intestinal FXR resulted in a decreased serum ceramide pool (Figure 1N). In the clinic, circulating ceramide levels were increased in patients with hypercholesterolemia (Figure 1O). In addition, serum FGF19 levels were positively related to serum total ceramide levels in humans (Figure 1P), indicating that activation of intestinal FXR may contribute to increases in circulating ceramide levels in humans. HCD-fed *Fxr^{fl/fl} ApoE^{-/-}* mice were supplemented daily with C16:0 ceramide by i.p. injection to determine whether ceramide has profound effects in vivo that compensate for the loss of intestinal FXR-derived improvements in atherosclerosis. After C16:0 ceramide administration, the ileal and serum ceramide profiles of *Fxr^{fl/fl} ApoE^{-/-}* mice recovered to levels similar to those of control mice (Figure 2, A and B). C16:0 ceramide had no effect on the expression of FXR signaling molecules (Supplemental Figure 3A). Indicators of insulin resistance were not significantly changed (Supplemental Figure 3, B–D). The reductions in lesion areas in the whole aortas and aortic roots of *Fxr^{fl/fl} ApoE^{-/-}* mice were largely reversed by C16:0 ceramide administration (Figure 2, C–F). In addition, the improvements in vascular IL-1 β ⁺ and CD36⁺ macrophage accumulation and systemic proinflammatory cytokine levels in the absence of intestinal FXR were completely eliminated after replenishment of C16:0 ceramide (Figure 2, G–K, and Supplemental Figure 3, E–J). However, C16:0 ceramide supplementation did not reverse the lower chole-

sterol levels in *Fxr^{fl/fl} ApoE^{-/-}* mice (Supplemental Figure 3, K–M). In conclusion, increased ceramide levels mediate the proatherogenic effects of intestinal FXR, especially aortic inflammation.

Taken together, the data indicate that the lack of intestinal FXR signaling on the *ApoE^{-/-}* background reduces the serum ceramide pool, which contributes to reductions in aortic inflammation during atherosclerosis progression.

***Smpd3* is an intestinal FXR target gene.** To explore how intestinal FXR modulates the serum ceramide pool, we determined the relative expression of genes involved in ceramide metabolism in the ileum of HCD-fed *Fxr^{fl/fl} ApoE^{-/-}* and *Fxr^{fl/fl} ApoE^{-/-}* mice. The relative mRNA levels of *Smpd3*, which participates in sphingomyelin hydrolysis to produce ceramides, and *Cers2*, which is involved in de novo ceramide synthesis, were lower in *Fxr^{fl/fl} ApoE^{-/-}* mice than in *Fxr^{fl/fl} ApoE^{-/-}* mice (Supplemental Figure 4, A and B). The ceramide salvage pathway and ceramide catabolism pathway were not different between the two groups (Supplemental Figure 4C). To further determine the function of intestinal FXR in ceramide metabolism, the relative expression of genes involved in ceramide metabolism was measured in mice treated with the potent FXR agonist GW4064 in vivo and in GW4064-treated intestinal organoids in vitro. In vivo, 1 week of GW4064 treatment by daily gavage increased intestinal FXR signaling and significantly elevated *Smpd3* mRNA levels in HCD-fed *Fxr^{fl/fl} ApoE^{-/-}* mice but not in *Fxr^{fl/fl} ApoE^{-/-}* mice (Supplemental Figure 4, D–G). In ileal organoids, activation of FXR via GW4064 treatment upregulated *Smpd3* mRNA expression (Supplemental Figure 5, A and B). Furthermore, intestinal organoids derived from *Fxr^{fl/fl}* and *Fxr^{fl/fl}* mice were used to determine whether GW4064-induced *Smpd3* mRNA expression depends on intestinal FXR. GW4064 increased *Smpd3* mRNA expression in ileal organoids isolated from *Fxr^{fl/fl}* mice but not in those isolated from *Fxr^{fl/fl}* mice (Figure 3, A and B). Based on these results, *Smpd3* may be an intestinal FXR target gene. Analysis of a database of chromatin immunoprecipitation followed by sequencing (ChIP-seq) of intestinal FXR (30) revealed 2 peaks for FXR binding sites in intron 2 of *Smpd3* (FXRE1 [+57611/+57623]: 5'-AGATCAGTGAAC-3' and FXRE2 [+58669/+58681]: 5'-GGGCATTGACCT-3') that are potentially associated with *Smpd3* transcription (Supplemental Figure 5C). Thus, a ChIP assay was performed on organoids isolated from vehicle-treated mice and GW4064-treated mice to confirm whether FXR binds to this site. FXR directly bound to the FXRE2 region but not the FXRE1 region (Figure 3C). Since FXRE2 is located in intron 2 of *Smpd3*, not the promoter region, it may be an enhancer of *Smpd3*. To test this possibility, the sequences 100 bp upstream and 100 bp downstream of FXRE1 (*Smpd3*-FXRE1) or FXRE2 (*Smpd3*-FXRE2) were inserted into the pGL4.27 luciferase reporter plasmid with a minimal promoter, and the enhancer activity was measured (Figure 3D). Only in *Smpd3*-FXRE2-transfected HCT116 cells did activation of FXR by GW4064 treatment induce transcription of the reporter gene (Figure 3E). When FXRE2 was deleted, there was no increase in reporter gene activity after GW4064 treatment (Figure 3F). These data demonstrate that the FXRE2 region in the *Smpd3* gene can bind to FXR and has enhancer activity. To further explore whether FXR mediates the interaction of the FXRE1/2 region with the *Smpd3* promoter region, a chromosome conformation capture

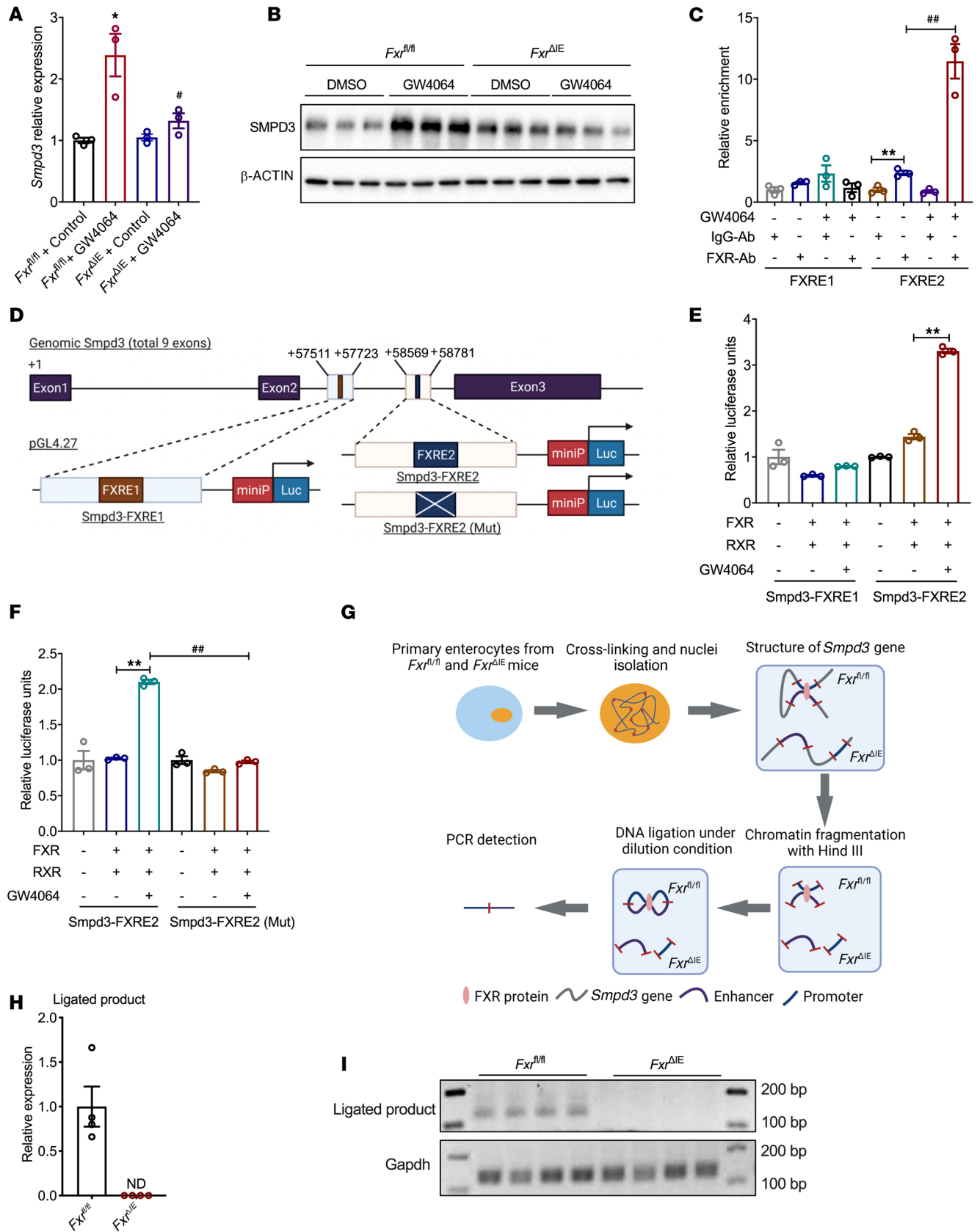


Figure 3. *Smpd3* is a target gene of intestinal FXR. (A and B) *Smpd3* mRNA (A) and SMPD3 protein levels (B) in ileal organoids from *Fxr^{fl/fl}* and *Fxr^{ΔIE}* mice treated with GW4064 (10 μM) or DMSO (*n* = 3/group). (C) ChIP assay on ileal organoids from vehicle- or GW4064-treated (10 mg/kg) mice; the organoids were treated with DMSO or GW4064 (10 μM) during culture (*n* = 3/group). (D) Construction of the pGL4.27 plasmids with FXRE1, FXRE2, and mutant FXRE2 (mut). (E and F) Luciferase reporter gene assays (*n* = 3/group). (G) Schematic diagram of the 3C assay procedure. (H and I) qPCR (H) and gel analysis (I) of the ligated DNA product (*n* = 4/group). ND, not detectable. The data are presented as the mean ± SEM. One-way ANOVA with Tukey's post hoc test: **P* < 0.05 versus *Fxr^{fl/fl}* + vehicle and #*P* < 0.05 versus *Fxr^{fl/fl}* + GW4064 (A); ***P* < 0.01 and ###*P* < 0.01 (C, E, and F). Unedited Western blots from which the data in panel A were derived and complete images of ligated products and Gapdh from which the data in panel I were derived are shown in Supplemental Figure 10.

(3C) assay (Figure 3G) was conducted using primary enterocytes isolated from GW4064-treated *Fxr^{fl/fl}* and *Fxr^{ΔIE}* mice (Supplemental Figure 5D). An interaction between the *Smpd3* promoter and the FXRE2 enhancer was detected in wild-type (WT) cells, while neither quantitative PCR (qPCR) nor gel analysis revealed a detectable ligated DNA product in the absence of FXR (Figure 3, H and I). These data indicate that FXR binds to an intron-localized enhancer to regulate *Smpd3* transcription.

To further explore whether SMPD3 is involved in FXR-induced ceramide production and secretion in the intestine, ileal organoids were employed. Activation of FXR increased ceramide levels in both organoids and culture supernatants, while treatment with the SMPD3 inhibitor GW4869 decreased the lev-

els (Figure 4, A and B). Additionally, an SMPD3-expressing lentivirus (LV-SMPD3) and a GFP-expressing lentivirus (LV-GFP) were generated to overexpress SMPD3 in organoids and in vivo. LV-SMPD3 infection attenuated the decrease in *Smpd3* expression in *Fxr^{ΔIE}* organoids without influencing the expression of other FXR target genes, namely, *Fgf15* and *Shp* (Figure 4C). In *Fxr^{ΔIE}* organoids, ceramide production and secretion were notably reduced, but the reductions could be reversed by overexpression of SMPD3 (Figure 4, D and E). As a target gene of FXR, *Smpd3* is responsible for FXR-induced ceramide production and secretion in the intestine.

Intestinal SMPD3 overexpression eliminates intestinal FXR-KO-mediated beneficial effects in atherosclerosis. To further confirm whether the intestinal FXR-mediated improvement in atherosclerosis is dependent on intestinal SMPD3, LV-SMPD3 was locally introduced into *Fxr^{ΔIE} ApoE^{-/-}* mice via surgery. SMPD3 was specifically overexpressed in the ileum, and there were no changes in neutral sphingomyelinase (N-SMase) activity in the liver or adipose tissue (Figure 5, A and B, and Supplemental Figure 6, A–C). Forced SMPD3 expression attenuated the decreases in intestinal ceramide production and serum ceramide levels caused by intestinal FXR KO, and restored the levels to near-control values (Figure 5, C and D). In *Fxr^{ΔIE} ApoE^{-/-}* mice, the reductions in lesion area were partially reversed by overexpression of SMPD3 in both whole aortas and cross sections of aortic roots (Figure 5, E–H). Treatment with LV-SMPD3 had no influence on insulin resistance or on liver and serum cholesterol levels (Supplemental Figure 6, D–I). Mac-2 staining showed higher macro-

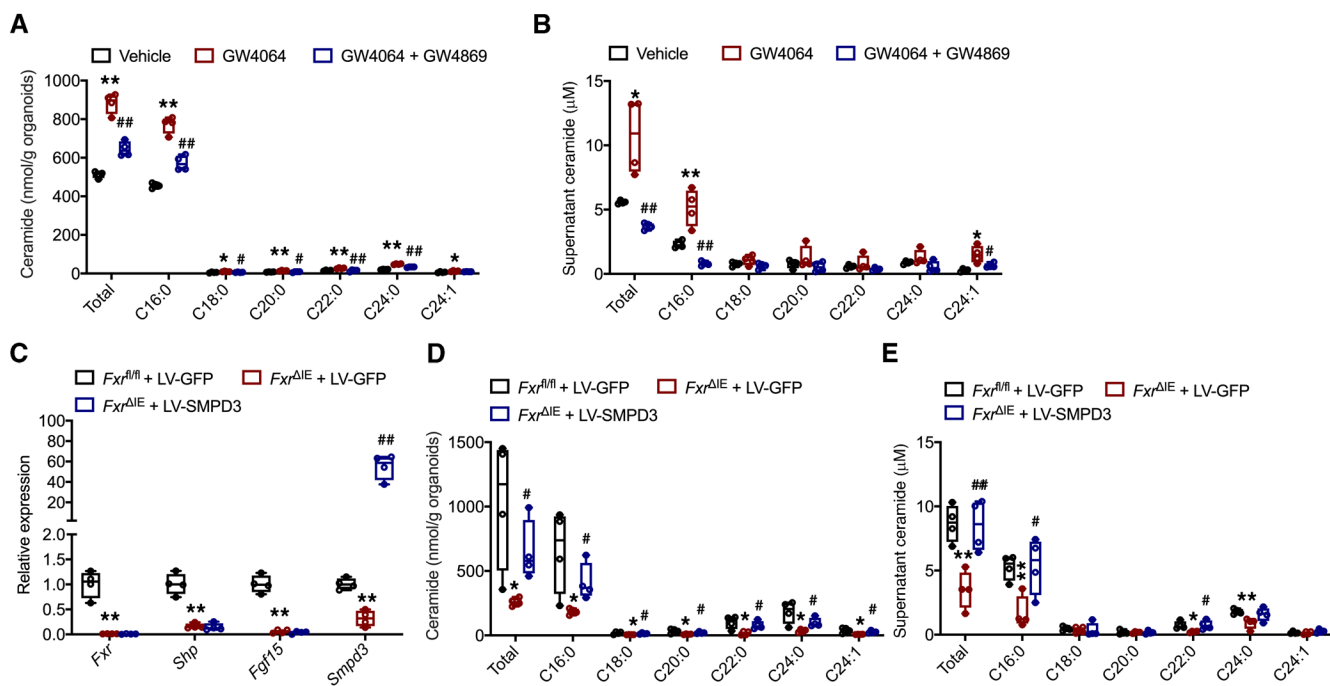


Figure 4. Ceramide level alterations are reversed by forced expression of SMPD3. (A and B) Levels of ceramides in ileal organoids treated with DMSO, GW4064 (10 μM), and GW4064 (10 μM) plus GW4869 (10 μM) (A) and in culture medium (B) (*n* = 4/group). (C) *Fxr*, *Shp*, *Fgf15*, and *Smpd3* mRNA levels in ileal organoids from *Fxr^{fl/fl}* and *Fxr^{ΔIE}* mice treated with LV-GFP or LV-SMPD3 (*n* = 4/group). (D and E) Levels of ceramides in ileal organoids (D) and in culture medium of tissues (E) isolated from *Fxr^{fl/fl}* and *Fxr^{ΔIE}* mice treated with LV-GFP or LV-SMPD3 (*n* = 4/group). The data are presented as the mean ± SEM. Kruskal-Wallis test with Dunn's post hoc test: **P* < 0.05, ***P* < 0.01 versus vehicle and #*P* < 0.05, ##*P* < 0.05 versus GW4064 (A and B); **P* < 0.05, ***P* < 0.01 versus *Fxr^{fl/fl}* + LV-GFP and #*P* < 0.05, ##*P* < 0.05 versus *Fxr^{ΔIE}* + LV-GFP (C–E).

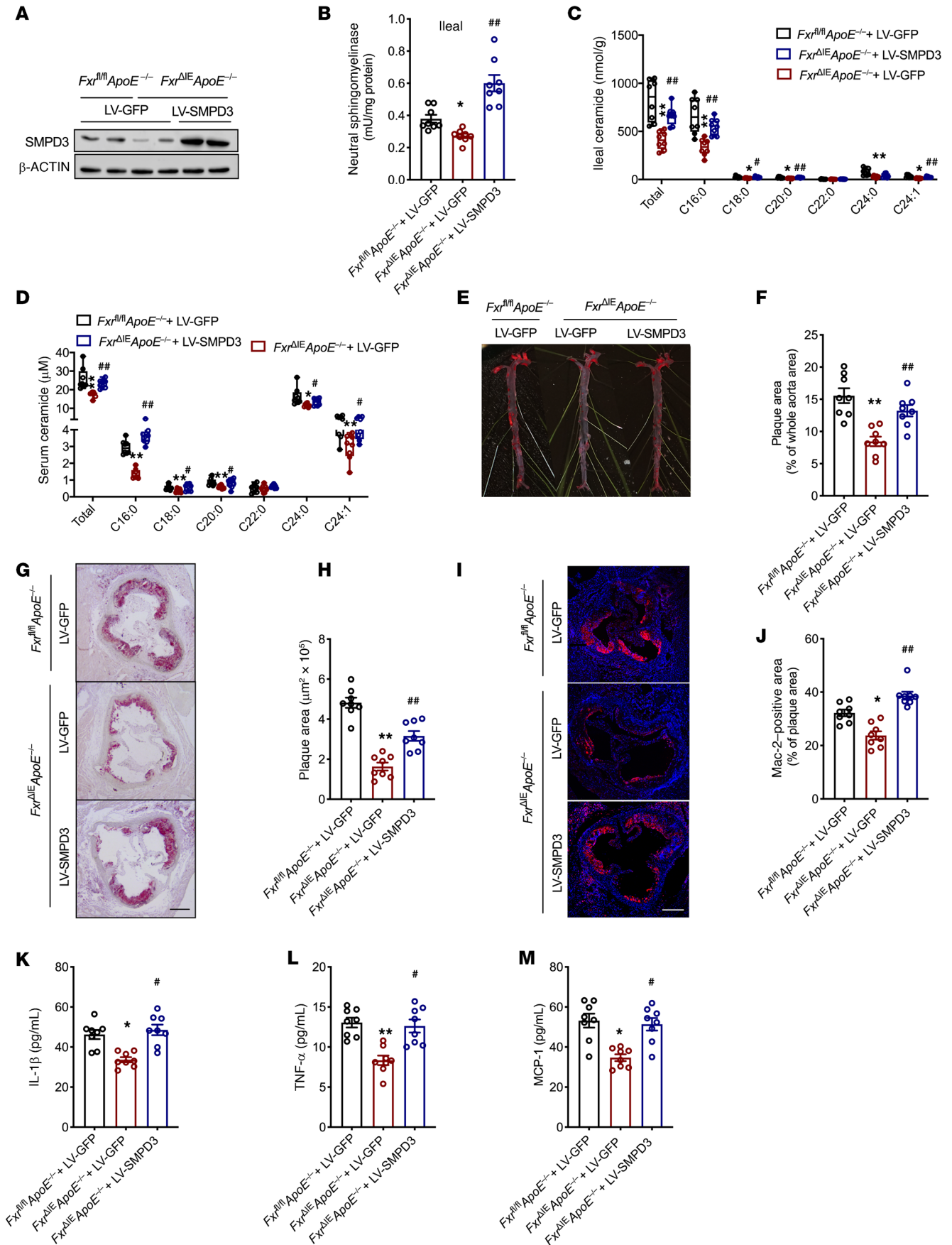


Figure 5. Forced expression of SMPD3 in the intestine negates FXR deficiency-mediated protection from atherosclerosis. *Fxr^{fl/fl} ApoE^{-/-}* and *Fxr^{ΔIE} ApoE^{-/-}* mice were surgically transfected with LV-GFP or LV-SMPD3 in the intestine, and then the mice were fed an HCD for 5 weeks ($n = 8/\text{group}$). (A and B) SMPD3 protein levels (A) and N-SMase activity (B) in the ileum. (C and D) Levels of ceramides in the ileum (C) and serum (D). (E and F) Representative images of aortas stained with Oil Red O (E) and quantification of the lesions (F). (G and H) Representative sections of left ventricular outflow tracts stained with Oil Red O (G) and the quantified lesion areas (H). (I and J) Immunofluorescence staining of atherosclerotic lesions for Mac-2 (I) and quantification of the positive areas (J). (K–M) Serum levels of the proinflammatory cytokines IL-1 β (K), TNF- α (L), and MCP-1 (M). The data are presented as the mean \pm SEM. One-way ANOVA with Tukey's post hoc test (B, F, H, and J–M) and Kruskal-Wallis test with Dunn's post hoc test (C and D): * $P < 0.05$, ** $P < 0.01$ versus *Fxr^{fl/fl} ApoE^{-/-}* + LV-GFP and # $P < 0.05$, ### $P < 0.01$ versus *Fxr^{ΔIE} ApoE^{-/-}* + LV-GFP. Scale bars: 200 μm . The unedited Western blots from which the data in panel A were derived are shown in Supplemental Figure 10.

phage infiltration in LV-SMPD3-treated *Fxr^{ΔIE} ApoE^{-/-}* mice than in LV-GFP-treated mice (Figure 5, I and J). In addition, the reductions in serum IL-1 β , TNF- α , and MCP-1 levels were attenuated by forced SMPD3 overexpression (Figure 5, K–M). Serum IL-10 and IL-12 levels were unchanged (Supplemental Figure 6, J and K). These data indicate that upregulation of intestinal SMPD3 mainly induces intestinal ceramide production and secretion without influencing circulating cholesterol levels, resulting in increased proinflammatory cytokine levels in the context of accelerated atherosclerosis.

GUDCA mitigates atherosclerosis via an intestinal FXR signaling-dependent mechanism. Glycoursodeoxycholic acid (GUDCA) has previously been identified as a natural antagonist of intestinal FXR (31). To clarify whether GUDCA has antiatherosclerotic effects, GUDCA (30 mg/kg/d) was orally administered to HCD-fed *Fxr^{fl/fl} ApoE^{-/-}* and *Fxr^{ΔIE} ApoE^{-/-}* mice. Intestinal FXR signaling was inhibited by oral GUDCA supplementation (Supplemental Figure 7A). However, GUDCA did not show beneficial effects on insulin resistance in mice fed an HCD (Supplemental Figure 7, B–D). Analysis of whole aortas and sections demonstrated that after 5 weeks of HCD feeding, the GUDCA-treated *Fxr^{fl/fl} ApoE^{-/-}* mice had smaller lesions than the vehicle-treated *Fxr^{fl/fl} ApoE^{-/-}* mice but not the *Fxr^{ΔIE} ApoE^{-/-}* mice (Figure 6, A–D). Mac-2 staining showed that GUDCA reduced macrophage infiltration in *Fxr^{fl/fl} ApoE^{-/-}* mice, but did not reduce macrophage infiltration in *Fxr^{ΔIE} ApoE^{-/-}* mice (Figure 6, E and F). Serum IL-1 β , TNF- α , and MCP-1 levels were decreased by GUDCA administration in *Fxr^{fl/fl} ApoE^{-/-}* mice, but no difference was found between the vehicle- and GUDCA-treated *Fxr^{ΔIE} ApoE^{-/-}* mice after 5 weeks of HCD feeding (Figure 6, G–I). Additionally, the IL-10 and IL-12 levels remained unchanged (Supplemental Figure 7, E and F). With GUDCA supplementation, intestinal *Smpd3* mRNA expression and SMPD3-mediated ceramide production and secretion were reduced in *Fxr^{fl/fl} ApoE^{-/-}* mice but not in *Fxr^{ΔIE} ApoE^{-/-}* mice (Figure 6, J–L, and Supplemental Figure 7G). Moreover, hepatic and serum cholesterol levels were reduced after GUDCA treatment in *Fxr^{fl/fl} ApoE^{-/-}* mice, but no further decreases were noted in GUDCA-treated *Fxr^{ΔIE} ApoE^{-/-}* mice compared to vehicle-treated *Fxr^{ΔIE} ApoE^{-/-}* mice fed an HCD (Supplemental Figure 7, H–J). The mRNA expression of cholesterol transport genes in the ileum was unchanged (Supplemental Figure

7K). Hepatic *Cyp7a1*, *Ldlr*, and *Abcg8* mRNA expression was upregulated in GUDCA-treated *Fxr^{fl/fl} ApoE^{-/-}* mice compared with vehicle-treated *Fxr^{fl/fl} ApoE^{-/-}* mice, whereas this effect was abrogated in *Fxr^{ΔIE} ApoE^{-/-}* mice (Supplemental Figure 7, L and M). These results suggest that GUDCA protects against atherosclerosis in a manner dependent on intestinal FXR signaling.

GUDCA and GW4869 can decrease further progression of developed atherosclerotic lesions. To explore whether selective inhibition of intestinal FXR and SMPD3 could be a therapeutic strategy for established atherosclerotic plaques, *ApoE^{-/-}* mice were fed an HCD for 5 weeks to induce atherosclerosis and then administered vehicle or GUDCA under chow diet treatment for an additional 3 weeks (Supplemental Figure 8A). As expected, FXR signaling in the ileum was suppressed by GUDCA treatment (Supplemental Figure 8B). En face staining of vessels and aortic root sections of atherosclerotic plaques with Oil Red O showed that GUDCA attenuated the progression of established atherosclerotic plaques without influencing glucose homeostasis (Figure 7, A–D, and Supplemental Figure 8, C–E). Compared with the vehicle, GUDCA decreased macrophage infiltration into plaques and attenuated the inflammatory response, as revealed by Mac-2 staining and serum proinflammatory cytokine levels (Figure 7, E–G, and Supplemental Figure 8, F and G). Although GUDCA treatment failed to increase hepatic CYP7A1-mediated cholesterol catabolism without HCD feeding (Supplemental Figure 8, H–K), intestinal N-SMase activity and ceramide levels in both the ileum and serum were markedly decreased in GUDCA-treated mice (Figure 7, H and I, and Supplemental Figure 8, L and M). In the absence of cholesterol stimulation during the treatment stage, GUDCA exerts its potential therapeutic effects on atherogenesis mainly by suppressing intestinal SMPD3-mediated ceramide production and secretion.

To further explore the potential of SMPD3 as a drug target, 10 mg/kg GW4869 was administered by daily gavage to chow diet-fed *ApoE^{-/-}* mice for 3 weeks after 5-week HCD treatment (Supplemental Figure 9A). Intestinal N-SMase activity was significantly inhibited after oral GW4869 treatment (Supplemental Figure 9B). GW4869 treatment reduced the lesion areas in aortas and roots without improving insulin resistance (Figure 7, J–M, and Supplemental Figure 9, C–E). Macrophage infiltration was lower in the GW4869-treated group than in the vehicle-treated group (Figure 7, N and O). The levels of IL-1 β , TNF- α , and MCP-1 were also decreased (Figure 7P and Supplemental Figure 9, F and G). Consistent with these findings, the levels of ileal and serum ceramides were markedly lower in the GW4869-treated group than in the vehicle-treated group (Figure 7, Q and R). However, cholesterol levels in both the liver and serum were not significantly different between the two groups (Supplemental Figure 9, H–J). Thus, inhibition of intestinal SMPD3-mediated ceramide production and secretion is a therapeutic strategy for treating atherosclerosis without influencing cholesterol levels.

Discussion

The pathologic process of atherosclerosis begins with trapping of cholesterol/lipoproteins in the vessel wall, which results in the expression of adhesion molecules and chemokines (e.g., MCP-1 and TNF- α). Then, macrophages are recruited to the vessel wall and differentiate into foam cells to scavenge excess

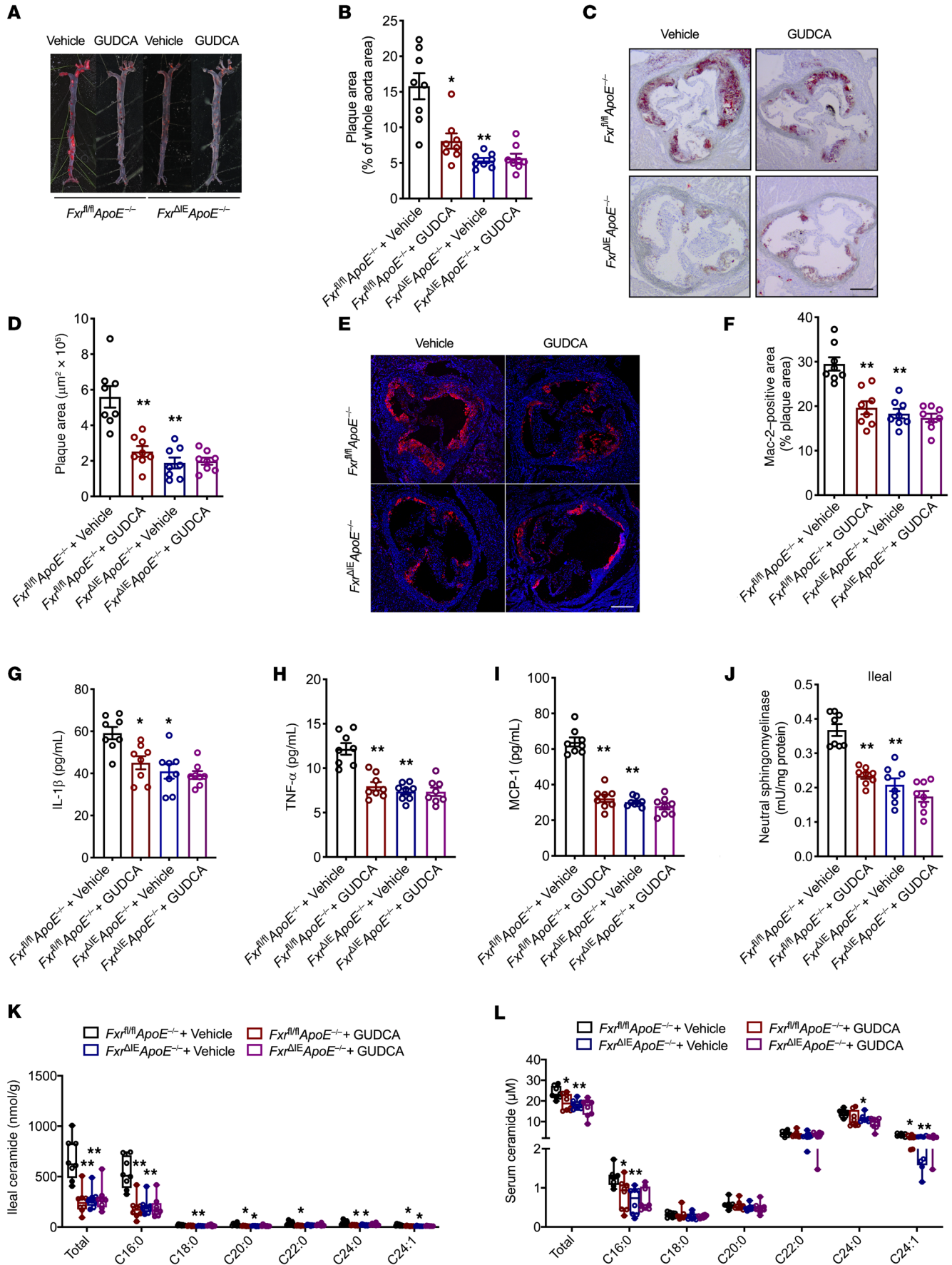


Figure 6. GUDCA treatment prevents atherosclerosis in a manner dependent on intestinal FXR signaling. HCD-fed *Fxr^{fl/fl} ApoE^{-/-}* and *Fxr^{dIE} ApoE^{-/-}* mice were given vehicle or GUDCA (30 mg/kg/d) by gavage for 5 weeks (*n* = 8/group). (A and B) Representative images of aortas stained with Oil Red O (A) and quantification of the lesions (B). (C and D) Oil Red O staining of left ventricular outflow tract sections (C) and the calculated plaque areas (D). (E and F) Typical left ventricular outflow tract sections stained for Mac-2 (E) and quantification of the positive areas (F). (G–I) Serum IL-1 β (G), TNF- α (H), and MCP-1 (I) levels. (J) N-SMase activity in the ileum. (K and L) Levels of ceramides in the ileum (K) and serum (L). The data are presented as the mean \pm SEM. One-way ANOVA with Tukey's post hoc test (B, D, and F–J) and Kruskal-Wallis test with Dunn's post hoc test (K and L): **P* < 0.05, ***P* < 0.01 versus *Fxr^{fl/fl} ApoE^{-/-}* + vehicle. Scale bars: 200 μ m.

lipids, producing inflammatory molecules (32). Therefore, the numbers of macrophages in atherosclerotic lesions and the levels of proinflammatory cytokines released into the circulation are representative of the severity and progression of atherosclerosis (33). In addition to cholesterol, sphingolipids also play a crucial role in chronic inflammation (34), and ceramide levels were found to be elevated in human atherosclerotic plaques (15). Notably, recent clinical studies demonstrated that circulating ceramides, including C16:0, C18:0, and C24:1, are independent predictors of adverse cardiovascular events resulting from unstable atherosclerotic plaques (11, 35, 36). Most existing therapies are designed to reduce the levels of cholesterol, but equally important molecules, namely, proinflammatory circulating lipids such as ceramides, have not been adequately addressed (37). Activation of the NLRP3 inflammasome was identified as a main trigger for chronic inflammation in atherosclerotic plaques (38). Ceramide was found to increase the nuclear translocation of NF- κ B in human microvascular EC line 1 and caspase 1 cleavage in macrophages (13, 39), indicating that ceramide could both increase *Nlrp3* and *Il1b* transcription (first signaling) and activate the NLRP3 inflammasome (second signaling). In addition, ceramide could facilitate fatty acid uptake by increasing CD36 in liver (40, 41). In the current study, FXR deficiency downregulated *Nlrp3*, *Il1b*, and *Cd36* mRNAs encoding macrophage markers in aortas, which could be reversed by administration of C16:0 ceramide.

FXR, a ligand-activated nuclear receptor that regulates bile acid synthesis, transport, and enterohepatic circulation, was found to play critical roles in metabolic diseases (6). Notably, inhibition of intestinal FXR signaling protects against high-fat diet-induced metabolic diseases, including obesity, insulin resistance, and fatty liver (25, 26, 42). However, the roles of intestinal FXR in the pathogenesis of hypercholesterolemia and atherosclerosis remain elusive. Although the potent FXR agonist OCA exerts some potential protective effects against the initiation and progression of atherosclerosis by elevating fecal cholesterol excretion and macrophage reverse cholesterol transport dependent on hepatic FXR activation (6), the roles of FXR signaling in other tissues, especially in the intestine, need to be further explored. Activation of intestinal FXR induces FGF15/19 expression and release into the blood, after which it travels to the liver to bind FGFR4 where it triggers a signaling pathway that inhibits *Cyp7a1* transcription (43). The *Cyp7a1* gene encodes cholesterol 7 α -hydroxylase, the key rate-limiting cho-

lesterol catabolic enzyme involved in bile acid synthesis (43). Accordingly, inhibiting intestinal FXR signaling relieves the suppression of *Cyp7a1* transcription and cholesterol catabolism in the liver. Recent studies have shown that *Cyp7a1* gene polymorphisms modify the risk of coronary artery disease and that deficiency of this gene triggers hypercholesterolemia in humans (44, 45). Furthermore, *Cyp7a1^{-/-}* mice have higher proatherogenic lipid levels than WT mice (46), and transgenic expression of CYP7A1 prevents atherosclerosis (47, 48). In addition to the obvious upregulation of *Cyp7a1* gene expression, an increase in *Ldlr* and *Abcg8* mRNA expression was also observed in the current study. This outcome was most likely the result of increased cholesterol catabolism (47). Although previous evidence suggests that intestinal FXR regulates intestinal ceramide levels, the underlying mechanism remains elusive (26). SMPD3 is the key enzyme catalyzing the hydrolysis of sphingomyelin to form ceramides and phosphocholine, and it is activated by unsaturated fatty acids and phosphatidylserine (49). It was reported that whole-body SMPD3 KO or GW4869 treatment ameliorated atherosclerosis, accompanied by decreased macrophage-mediated inflammation (50). Notably, SMPD3 in vascular cell types could directly influence secretion of inflammatory cytokines in macrophages and expression of adhesion molecules in ECs (50). In the current study, SMPD3 was verified to be encoded by an FXR target gene and was found to mediate the FXR inhibition-induced beneficial effects on intestinal ceramide secretion.

Bile acids are recognized as small signaling molecules that maintain an organism's macronutrient metabolism and energy balance (51). GUDCA is an endogenous FXR antagonist in humans that shows potential therapeutic effects against obesity-induced metabolic diseases (31). In this study, an HCD significantly activated intestinal FXR signaling in both humans and mice. Disruption or inhibition of FXR in the intestine rescued hepatic CYP7A1 expression and decreased serum cholesterol levels by promoting hepatic cholesterol elimination. Additionally, intestinal FXR binds to an intron-localized enhancer to upregulate *Smpd3* transcription and accelerate ileal ceramide production. GUDCA treatment was found to have preventive and therapeutic effects against atherosclerosis that were dependent on the inhibition of intestinal FXR signaling. After cholesterol stimulation was withdrawn, GUDCA treatment exerted further therapeutic effects on atherosclerosis, primarily by reducing circulating proinflammatory ceramide levels without influencing serum cholesterol levels. Inhibition of SMPD3 with GW4869 had similar therapeutic effects on atherosclerosis.

In conclusion, serum ceramide levels can be used as clinical biomarkers for the diagnosis and treatment of atherosclerosis. Based on this finding, the present study reveals that intestinal FXR inhibition can both control hypercholesterolemia and reduce ceramide levels. For patients with well-managed cholesterol, suppression of intestinal SMPD3 could be tested as a therapeutic strategy for atherosclerosis treatment.

Methods

Human subjects. The study included 30 healthy subjects and 30 patients with hypercholesterolemia, and hypercholesterolemia was defined by a high TC level (≥ 6.2 mmol/L). The demographic char-

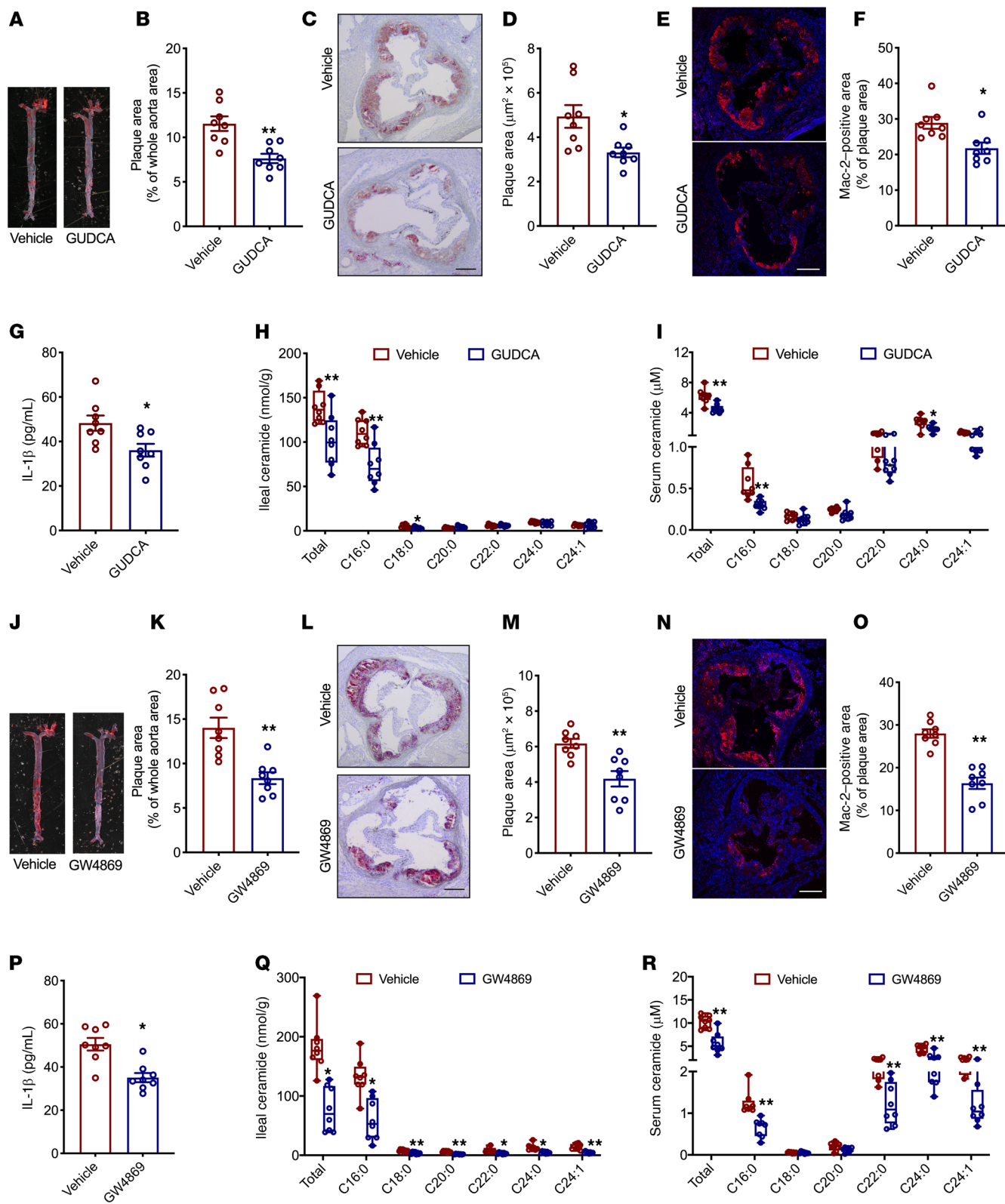


Figure 7. Oral GUDCA or GW4869 administration postpones progression of established atherosclerotic lesions. *ApoE*^{-/-} mice were fed an HCD for 5 weeks, and vehicle or GUDCA was administered by gavage under chow diet feeding for another 3 weeks (*n* = 8/group). (A and B) Representative images (A) and quantification (B) of aortic plaque areas. (C and D) Representative Oil Red O–stained sections of left ventricular outflow tracts (C) and quantification of the plaque areas (D). (E and F) Representative images of left ventricular outflow tract sections stained for Mac-2 (E) and statistical analysis of the Mac-2–positive areas (F). (G) Serum IL-1β levels. (H and I) Levels of ceramides in the ileum (H) and serum (I). *ApoE*^{-/-} mice were fed an HCD for 5 weeks and treated daily with GW4869 by gavage under chow diet feeding for another 3 weeks (*n* = 8/group). (J and K) Representative images (J) and quantification (K) of the aortic plaque areas. (L and M) Representative Oil Red O–stained cross sections of aortic roots (L) and quantification of the lesion areas (M). (N and O) Immunofluorescence staining for Mac-2 (N) and statistical analysis of the Mac-2–positive areas (O). (P) Serum IL-1β levels. (Q and R) Levels of ceramides in the ileum (Q) and serum (R). The data are presented as the mean ± SEM. Two-tailed Student's *t* test (B, D, F, G, K, M, O, and P) and Mann-Whitney *U* test (H, I, Q, and R): **P* < 0.05, ***P* < 0.01 versus vehicle. Scale bars: 200 μm.

acteristics of the subjects are listed in Supplemental Table 1. The exclusion criteria were familial hypercholesterolemia; pregnancy; severe diabetes; severe hepatic diseases; severe nephropathy; organic digestive diseases; autoimmune diseases; cancer; infectious diseases, including pulmonary tuberculosis and AIDS; alcoholism; continuous antibiotic use for over 3 days within 3 months prior to enrollment; continuous use of a weight-loss drug for over 1 month; and gastrointestinal surgery (except for appendicitis or hernia surgery). All clinical information was collected according to standard procedures. The collected metadata covered participants' anthropometric features and information related to health status, age, sex, disease history, medication, gastrointestinal conditions, dietary habits, sleep situation, and physical activity. Peripheral blood samples were centrifuged at 1000g for 5 minutes after standing at room temperature for at least 30 minutes to obtain the serum. The levels of triglycerides, TC, high-density lipoprotein cholesterol, and low-density lipoprotein cholesterol were measured using an autoanalyzer (BioTek Instruments 800TS).

Mice. All mice were maintained in a specific pathogen–free (SPF) environment. An HCD (Research Diets, D12109C) was used to feed 8-week-old male mice for 5 weeks to induce atherosclerosis. *Fxr*^{fl/fl} and *Fxr*^{ΔIE} mice (52) were crossed with *ApoE*^{-/-} mice (male 5-week-old *ApoE*^{-/-} mice were obtained from the Department of Laboratory Animal Science at Peking University) to generate *Fxr*^{fl/fl} *ApoE*^{-/-} and *Fxr*^{ΔIE} *ApoE*^{-/-} mice, which were used to explore the role of intestinal FXR in the progression of atherosclerosis. For the 2-group experiment, 8-week-old male *Fxr*^{fl/fl} *ApoE*^{-/-} and *Fxr*^{ΔIE} *ApoE*^{-/-} mice were fed an HCD for 5 weeks. In 4-group studies, HCD-fed *Fxr*^{fl/fl} *ApoE*^{-/-} and *Fxr*^{ΔIE} *ApoE*^{-/-} mice were given vehicle or 50 mg/kg/d GUDCA (Sigma-Aldrich, 06863) by gavage. In the 5-week C16:0 ceramide administration model, *Fxr*^{ΔIE} *ApoE*^{-/-} mice were given vehicle or C16:0 ceramide (10 mg/kg/d) by i.p. injection every day. To investigate the therapeutic effects of GUDCA and GW4869 on atherosclerosis, *ApoE*^{-/-} mice were fed an HCD for 5 weeks, and then the mice were fed a chow diet and were given vehicle, GUDCA (30 mg/kg/d), or GW4869 (30 mg/kg/d, Selleck Chemicals, S7609) for another 3 weeks. For short-term treatment, *Fxr*^{fl/fl} *ApoE*^{-/-} and *Fxr*^{ΔIE} *ApoE*^{-/-} mice received 10 mg/kg/d GW4064 (Sigma-Aldrich, G5172) orally for 1 week. To overexpress SMPD3 in the ileum, mice

received a small intestinal lentiviral injection as described previously (53). In brief, the small intestine was elevated from 6–8 cm distal to the cecum and was ligated with clamps at both ends to restrict outward flow of virus and inward flow of intestinal fluids. A longitudinal 3-mm incision was made in the intestinal section, and the section was then flushed with saline via an insulin needle inserted immediately below the clamp 6 cm from the cecum. Then, 0.2 mL of lentivirus expressing a mismatch sequence or HBLV-m-SMPD3 (Hanbio Biotechnology) was administered via the insulin needle. Twenty minutes later, the intestine was flushed with saline, and the clamps were removed. Finally, the incision was sutured with 10-0 suture and after 3 days HCD feeding was initiated. The mice were fed the HCD for 5 weeks to induce atherosclerosis.

Organoid culture, lentiviral transduction, and treatment. Small intestines were isolated from *Fxr*^{fl/fl} *ApoE*^{-/-} and *Fxr*^{ΔIE} *ApoE*^{-/-} mice, dissected, and washed with Dulbecco's PBS 10 times. Then, the intestinal fragments were incubated with Gentle Cell Dissociation Reagent (STEMCELL Technologies) to separate the crypts and villi from the intestinal basement membrane. After centrifugation, the crypts were isolated and resuspended in a 1:1 mixture of Matrigel (Corning) and IntestiCult organoid growth medium (OGM) (STEMCELL Technologies) at a density of 6000 crypts/mL. A droplet of 50 μL containing 300 crypts was placed into the center of each well of a prewarmed 24-well plate, forming a dome. After the domes had solidified, 750 μL of OGM was added to each well. The crypts were cultured at 37°C under 5% CO₂, and the medium was refreshed every 3 days. For organoid lentiviral transduction, organoids were harvested and placed into 15 mL tubes. The supernatant was removed by centrifugation, and HBLV-m-SMPD3 (1 × 10⁶ PFU/100 crypts) was added. The organoid-virus mixture was placed in an incubator for 1 hour at 37°C to allow transduction. Finally, the organoids were plated and cultured as mentioned above. To examine the production of ceramides, intestinal epithelial organoids were cultured in OGM as described above for 7 days and cultured with GW4064 (10 μM) for 3 days before being harvested for RNA and protein extraction.

Analysis of atherosclerotic plaques. Whole aorta and left ventricular outflow tract samples were obtained after perfusion with PBS. After fixation with 4% paraformaldehyde for 4–6 hours, these tissues were dehydrated in a 20% sucrose solution. The left ventricular outflow tract samples were embedded in OCT compound to acquire frozen sections. Then, the aortas and frozen sections were stained with Oil Red O and quantified using ImageJ software (NIH). The frozen sections were stained with antibodies against Mac-2 (CL8942AP, Cedarlane), IL-1β (A19635, ABclonal), or CD36 (A1470, ABclonal). Alexa Fluor 546–conjugated anti-rat (DDXCR05A546, Novus) and Alexa Fluor 647–conjugated anti-rabbit (Ab150075, Abcam) antibodies were used as secondary antibodies.

Biochemical and immunological assays. Serum cholesterol and triglyceride levels were quantified with commercial kits (Biosino Bio-Technology). Liver tissues (~20 mg) were homogenized in triglyceride extraction buffer (E1003, Applygen), and the supernatants were used to measure the cholesterol and triglyceride concentrations, which were normalized to the liver weights. Serum inflammatory cytokines were detected using an inflammation cytometric bead array kit (552364, BD Biosciences). Serum FGF19 levels were measured with a Human FGF-19 Quantikine ELISA Kit (DF1900, R&D Systems).

Metabolic assays. For a glucose tolerance test, mice were fasted for 16 hours and then injected with 1 g/kg glucose. For an insulin tolerance test, mice were fasted for 4 hours and then injected with insulin (I8040, Solarbio) at a dose of 1 U/kg. Blood samples were taken from the tail at 0, 15, 30, 60, and 90 minutes after injection, and the glucose concentration was measured using a glucometer (Contour TS, Bayer). The fasting insulin concentration was measured with an insulin ELISA kit (SEKR-0141, Solarbio).

N-SMase activity. Ileal, hepatic, and adipose tissues were collected for N-SMase activity measurement using an Amplex Red Sphingomyelinase Assay Kit (A12220, Invitrogen). The results were normalized to the protein concentrations.

Lipidomics analysis. For serum lipidomics analysis, 50 μ L of serum was mixed with 200 μ L of a cold chloroform/methanol (2:1) solution containing 1 μ M LM6002 (Avanti Polar Lipids) as an internal standard. The mixture was vortexed for 30 seconds and centrifuged at 15,000g for 5 minutes at 4°C, and then the lower organic phase was collected and evaporated. For ileal tissue lipidomics analysis, approximately 20 mg of ileal tissue was homogenized with 200 μ L of H₂O and then extracted with 1000 μ L of a cold chloroform/methanol (2:1) solution containing 1 μ M LM6002 as an internal standard. Each sample was vortexed for 30 seconds, incubated at room temperature for 30 minutes, and centrifuged at 15,000g for 20 minutes at 4°C. The lower organic phase was collected and evaporated. The residue was dissolved in 100 μ L of isopropanol/acetonitrile (IPA/ACN) (1:1). The samples were analyzed with an Eksigent LC100 and an AB SCIEX TripleTOF 5600 system using a Waters XBridge Peptide BEH C18 column (3.5 μ m, 2.1 \times 100 mm) under the following conditions: UPLC: A, 10 mM ammonium formate and 0.1% formic acid in water; B, 10 mM ammonium formate and 0.1% formic acid in 49.9% ACN and 49.9% IPA; gradient: 35% B at 0 minutes, 80% B at 2 minutes, 100% B at 9 minutes, 100% B at 15 minutes, 35% B at 16 minutes, and 35% B at 20 minutes; flow rate, 0.4 mL/min; and injection volume, 2 μ L. The lipid metabolites were identified by comparing the parent ion masses and MS/MS fragment masses to the acknowledged database LIPID MAPS (<https://www.lipidmaps.org/>). Peak extraction and integration were performed with PeakView 1.2 software (<https://sciex.com/products/software/peakview-software>). Principal component analysis (PCA), PLS-DA, and variable importance for the projection (VIP) scoring were carried out using MetaboAnalyst 3.0 (<https://www.metaboanalyst.ca/>). For quantification of ceramide metabolites, the data were analyzed with MultiQuant 2.1 software (AB SCIEX). Lipid standards were purchased from Avanti Polar Lipids.

Fast-performance liquid chromatography. To assess serum cholesterol/lipoprotein profiles, pooled serum (100 μ L) was analyzed by FPLC on a Superose S-6 10/300 GL column at a flow rate of 0.5 mL/min. Forty fractions (0.5 mL/fraction) were collected and measured with commercial kits (Biosino Bio-Technology).

Serum C4 analysis. Equal volumes of serum were mixed with ACN containing 1 μ M chlorpropamide (internal standard). The human serum samples were vortexed and then centrifuged 1000g for 10 minutes at 4°C to precipitate particulates. The supernatant of each sample was transferred to an autosampler vial, and 20 μ L was resolved by reversed-phase chromatography on a Prominence 20 UFLCXR system (Shimadzu) with a Waters BEH C18 column (100 mm \times 2.1 mm, 1.7 μ m particle size). The eluate was delivered into a 5600 TripleTOF using a Duospray ion source (SCIEX) operating in enhanced mode, and the transition m/z 401.3–177.1 was monitored.

Western blot analysis. Ileal tissues and ileal organoid samples were homogenized in RIPA buffer with protease and phosphatase inhibitors. The protein extracts were resolved by SDS-PAGE and transferred to PVDF membranes. The membranes were incubated with antibodies against SMPD3 (Santa Cruz, sc-166637) and β -actin (Abcam, ab8227) overnight at 4°C. The complete unedited Western blot images are shown in Supplemental Figure 10.

ChIP assay. Ileal organoids were isolated from *Fxr^{fl/fl}* and *Fxr^{ΔIE}* mice treated daily with 10 mg/kg GW4064 by gavage, and the organoids were also treated with 10 μ M GW4064 during culture in vitro. ChIP was performed using a SimpleChIP Plus Enzymatic Chromatin IP Kit (magnetic beads, Cell Signaling, 9005).

3C-qPCR. Single-cell preparations (primary enterocytes) were derived from *Fxr^{fl/fl}* (WT) and *Fxr^{ΔIE}* (KO) mice treated daily with 10 mg/kg GW4064 by gavage for 1 week. A 3C assay was conducted as described previously (54). In brief, 1×10^7 WT or KO primary enterocytes were cross-linked in a 1% formaldehyde solution at room temperature for 10 minutes and quenched with 125 mM glycine. Cells were lysed with cold lysis buffer to obtain nuclear pellets. The nuclei were lysed with Triton X-100, and the chromatin was further digested with the restriction enzyme HindIII (New England Biolabs). The digested DNA segments were ligated using 200 U of T4 DNA ligase for 4 hours at 16°C in diluted conditions. After decrosslinking, the DNA was purified and dissolved in Tris-HCl buffer for further qPCR and gel analyses.

Luciferase assay. HCT116 cells (ATCC, CCL-247) were cotransfected with mouse FXR/RXR expression vectors, pGL4.27 luciferase plasmids (containing the sequences 100 bp upstream and 100 bp downstream of FXRE1 [Smpd3-FXRE1] or FXRE2 [Smpd3-FXRE2], or a deletion mutant of Smpd3-FXRE2 with a minimal promoter) and a Renilla luciferase control vector (pRL-luciferase, Promega) using Lipofectamine 3000 transfection reagent (Thermo Fisher Scientific). Twenty-four hours after transfection, the cells were exposed to DMSO or 10 μ M GW4064. Luciferase assays were performed using a dual-luciferase assay system (Promega). Firefly and Renilla luciferase activity levels were measured by a Veritas microplate luminometer (Turner Biosystems).

Real-time PCR analysis. All tissue samples were snap-frozen in liquid nitrogen and stored at –80°C. TRIzol reagent (Invitrogen, 15596026) was used to isolate total RNA from the frozen tissues with a standard phenol/chloroform extraction protocol. Reverse transcription was conducted using a Reverse Transcription Kit (G490, ABM) with 2 μ g of total RNA to synthesize cDNA samples. The real-time PCR primer sequences are listed in Supplemental Table 2. The relative abundances of the involved genes were calculated by normalizing their levels to those of *18S* mRNA.

Statistics. All statistical data were analyzed with GraphPad Prism version 9.0. The sample distribution was determined by the Kolmogorov-Smirnov normality test. No data were excluded during the data analysis. All experimental data are reported as the mean \pm SEM. A 2-tailed Student's *t* test, Mann-Whitney *U* test, 1-way ANOVA with Tukey's post hoc test, Kruskal-Wallis test followed by Dunn's test, or Pearson's correlation analysis were applied for the mouse and clinical human samples. A *P* value of less than 0.05 was considered to indicate significance.

Study approval. The collection of human samples was approved by the Ethics Committee of Peking Union Medical College (PUMC) Hospital. All participants were recruited with informed consent through PUMC Hospital as part of the PUMC Aging Cohort of Willed Donation

(PACD) project between October 2018 and October 2019. All animal studies were approved by the Animal Research Ethics Committees of Peking University and the NIH.

Author contributions

QW, LS, XH, XW, FX, BC, XL, JX, PW, DA, Shaofei Zhang, GZ, CY, YY, and YZ performed the experiments and analyzed the data. CJ, FJG, Shuyang Zhang, and MB designed and supervised the study. LS, QW, and CJ wrote the manuscript. QW, LS, and XH contributed equally to this work. All authors edited the manuscript and approved the final manuscript.

Acknowledgments

This work was supported by the National Natural Science Foundation of China (no. 91857115); the National Key Research and Development Program of China (2018YFA0800700); the National Natural Science Foundation of China (nos. 31925021 and 81921001); the National Cancer Institute Intramural Research Program; the

National Institute of Diabetes and Digestive and Kidney Disease, NIH (U01DK119702); the Beijing Natural Science Foundation (no. 7202152); and the CAMS Innovation Fund for Medical Sciences (CIFMS) (nos. 2017-I2M-2-002, 2019-I2M-1-001, and 2016-I2M-1-002). DA was supported by the Faculty of Pharmaceutical Sciences, Fukuoka University.

Address correspondence to: Changtao Jiang, Department of Physiology and Pathophysiology, Peking University, Physiology Building, Room 324, 38 Xueyuan Road, Haidian District, Beijing, China, 100191. Phone: 81.10.82801440; Email: jiangchangtao@bjmu.edu.cn. Or to: Frank J. Gonzalez, NIH, NCI, Building 37, Room 3112, 9000 Rockville Pike, Bethesda, Maryland 20892, USA. Phone: 240.760.6875; Email: gonzalef@mail.nih.gov. Or to: Shuyang Zhang, Department of Cardiology, Peking Union Medical College Hospital, Academic Building, Room 901, No.1, Shuaifuyuan, Dongcheng District, Beijing, China, 100730. Phone: 81.10.69155810; Email: shuyangzhang103@nrdrs.org.

- Tunon J, et al. Interplay between hypercholesterolaemia and inflammation in atherosclerosis: translating experimental targets into clinical practice. *Eur J Prev Cardiol.* 2018;25(9):948–955.
- Lambert G, et al. The farnesoid X-receptor is an essential regulator of cholesterol homeostasis. *J Biol Chem.* 2003;278(4):2563–2570.
- Zhang Y, et al. FXR deficiency causes reduced atherosclerosis in *Ldlr^{-/-}* mice. *Arterioscler Thromb Vasc Biol.* 2006;26(10):2316–2321.
- Hanniman EA, et al. Loss of functional farnesoid X receptor increases atherosclerotic lesions in apolipoprotein E-deficient mice. *J Lipid Res.* 2005;46(12):2595–2604.
- Guo GL, et al. Effects of FXR in foam-cell formation and atherosclerosis development. *Biochim Biophys Acta.* 2006;1761(12):1401–1409.
- Xu Y, et al. Farnesoid X receptor activation increases reverse cholesterol transport by modulating bile acid composition and cholesterol absorption in mice. *Hepatology.* 2016;64(4):1072–1085.
- Qi Y, et al. PPAR alpha-dependent exacerbation of experimental colitis by the hypolipidemic drug fenofibrate. *Am J Physiol Gastrointest Liver Physiol.* 2014;307(5):G564–G573.
- Sniderman AD, et al. Hepatic cholesterol homeostasis: is the low-density lipoprotein pathway a regulatory or a shunt pathway? *Arterioscler Thromb Vasc Biol.* 2013;33(11):2481–2490.
- Chiang JY. Bile acid metabolism and signaling. *Compr Physiol.* 2013;3(3):1191–1212.
- Kong B, et al. Mechanism of tissue-specific farnesoid X receptor in suppressing the expression of genes in bile-acid synthesis in mice. *Hepatology.* 2012;56(3):1034–1043.
- Summers SA. Could ceramides become the new cholesterol? *Cell Metab.* 2018;27(2):276–280.
- Borodzicz S, et al. Sphingolipids in cardiovascular diseases and metabolic disorders. *Lipids Health Dis.* 2015;14:55.
- Vandanmagsar B, et al. The NLRP3 inflammasome instigates obesity-induced inflammation and insulin resistance. *Nat Med.* 2011;17(2):179–188.
- Boon J, et al. Ceramides contained in LDL are elevated in type 2 diabetes and promote inflammation and skeletal muscle insulin resistance. *Diabetes.* 2013;62(2):401–410.
- Edsfeldt A, et al. Sphingolipids contribute to human atherosclerotic plaque inflammation. *Arterioscler Thromb Vasc Biol.* 2016;36(6):1132–1140.
- Zhang X, et al. Adipocyte hypoxia-inducible factor 2 α suppresses atherosclerosis by promoting adipose ceramide catabolism. *Cell Metab.* 2019;30(5):937–951.
- Cheng JM, et al. Plasma concentrations of molecular lipid species in relation to coronary plaque characteristics and cardiovascular outcome: Results of the ATHEROREMO-IVUS study. *Atherosclerosis.* 2015;243(2):560–566.
- Laaksonen R, et al. Plasma ceramides predict cardiovascular death in patients with stable coronary artery disease and acute coronary syndromes beyond LDL-cholesterol. *Eur Heart J.* 2016;37(25):1967–1976.
- Wang DD, et al. Plasma ceramides, mediterranean diet, and incident cardiovascular disease in the PREDIMED Trial (Prevención con Dieta Mediterránea). *Circulation.* 2017;135(21):2028–2040.
- Chaurasia B, Summers SA. Ceramides — lipotoxic inducers of metabolic disorders. *Trends Endocrinol Metab.* 2015;26(10):538–550.
- Meeusen JW, et al. Plasma ceramides. *Arterioscler Thromb Vasc Biol.* 2018;38(8):1933–1939.
- Chai JC, et al. Association of lipidomic profiles with progression of carotid artery atherosclerosis in HIV infection. *JAMA Cardiol.* 2019;4(12):1239–1249.
- Senkal CE, et al. Ceramide is metabolized to acylceramide and stored in lipid droplets. *Cell Metab.* 2017;25(3):686–697.
- Correnti JM, et al. Pharmacological ceramide reduction alleviates alcohol-induced steatosis and hepatomegaly in adiponectin knockout mice. *Am J Physiol Gastrointest Liver Physiol.* 2014;306(11):G959–G973.
- Jiang C, et al. Intestine-selective farnesoid X receptor inhibition improves obesity-related metabolic dysfunction. *Nat Commun.* 2015;6:10166.
- Jiang C, et al. Intestinal farnesoid X receptor signaling promotes nonalcoholic fatty liver disease. *J Clin Invest.* 2015;125(1):386–402.
- Tabas I, Bornfeldt KE. Macrophage phenotype and function in different stages of atherosclerosis. *Circ Res.* 2016;118(4):653–667.
- Bennett MR, et al. Vascular smooth muscle cells in atherosclerosis. *Circ Res.* 2016;118(4):692–702.
- Gimbrone MA Jr., Garcia-Cardena G. Endothelial cell dysfunction and the pathobiology of atherosclerosis. *Circ Res.* 2016;118(4):620–636.
- Thomas AM, et al. Genome-wide tissue-specific farnesoid X receptor binding in mouse liver and intestine. *Hepatology.* 2010;51(4):1410–1419.
- Sun L, et al. Gut microbiota and intestinal FXR mediate the clinical benefits of metformin. *Nat Med.* 2018;24(12):1919–1929.
- Jagavelu K, et al. Systemic deficiency of the MAP kinase-activated protein kinase 2 reduces atherosclerosis in hypercholesterolemic mice. *Circ Res.* 2007;101(11):1104–1112.
- Daugherty A, et al. Recommendation on design, execution, and reporting of animal atherosclerosis studies: a scientific statement from the American Heart Association. *Circ Res.* 2017;121(6):e53–e79.
- Monteiro R, Azevedo I. Chronic inflammation in obesity and the metabolic syndrome. *Mediators Inflamm.* 2010;2010(18):289645.
- Havulinna AS, et al. Circulating ceramides predict cardiovascular outcomes in the population-based FINRISK 2002 cohort. *Arterioscler Thromb Vasc Biol.* 2016;36(12):2424–2430.
- Volmer D, et al. Perception of the professional knowledge of and education on the medical technology products among the pharmacists in the baltic and nordic countries—a cross-sectional exploratory study. *Pharmacy (Basel).* 2016;4(4):E29.
- Charo IF, Taub R. Anti-inflammatory therapeutics for the treatment of atherosclerosis. *Nat Rev Drug Discov.* 2011;10(5):365–376.
- Grebe A, et al. NLRP3 inflammasome and the IL-1 pathway in atherosclerosis. *Circ Res.* 2018;122(12):1722–1740.

39. Chen CL, et al. Anti-dengue virus nonstructural protein 1 antibodies cause NO-mediated endothelial cell apoptosis via ceramide-regulated glycogen synthase kinase-3 β and NF- κ B activation. *J Immunol*. 2013;191(4):1744-1752.
40. Xia JY, et al. Targeted induction of ceramide degradation leads to improved systemic metabolism and reduced hepatic steatosis. *Cell Metab*. 2015;22(2):266-278.
41. Chaurasia B, et al. Targeting a ceramide double bond improves insulin resistance and hepatic steatosis. *Science*. 2019;365(6451):386-392.
42. Zhang L, et al. Farnesoid X receptor signaling shapes the gut microbiota and controls hepatic lipid metabolism. *mSystems*. 2016;1(5):e00070-16.
43. Chiang JY. Recent advances in understanding bile acid homeostasis. *F1000Res*. 2017;6:2029.
44. Pullinger CR, et al. Human cholesterol 7 α -hydroxylase (CYP7A1) deficiency has a hypercholesterolemic phenotype. *J Clin Invest*. 2002;110(1):109-117.
45. Iwanicki T, et al. CYP7A1 gene polymorphism located in the 5' upstream region modifies the risk of coronary artery disease. *Dis Markers*. 2015;2015:185969.
46. Erickson SK, et al. Hypercholesterolemia and changes in lipid and bile acid metabolism in male and female cyp7A1-deficient mice. *J Lipid Res*. 2003;44(5):1001-1009.
47. Li T, et al. Transgenic expression of cholesterol 7 α -hydroxylase in the liver prevents high-fat diet-induced obesity and insulin resistance in mice. *Hepatology*. 2010;52(2):678-690.
48. Liu H, et al. Cholesterol 7 α -hydroxylase protects the liver from inflammation and fibrosis by maintaining cholesterol homeostasis. *J Lipid Res*. 2016;57(10):1831-1844.
49. Airola MV, et al. Structure of human nSMase2 reveals an interdomain allosteric activation mechanism for ceramide generation. *Proc Natl Acad Sci U S A*. 2017;114(28):E5549-E5558.
50. Lallemand T, et al. nSMase2 (type 2-neutral sphingomyelinase) deficiency or inhibition by GW4869 reduces inflammation and atherosclerosis in Apoe(-/-) mice. *Arterioscler Thromb Vasc Biol*. 2018;38(7):1479-1492.
51. Hylemon PB, et al. Bile acids as regulatory molecules. *J Lipid Res*. 2009;50(8):1509-1520.
52. Kim I, et al. Differential regulation of bile acid homeostasis by the farnesoid X receptor in liver and intestine. *J Lipid Res*. 2007;48(12):2664-2672.
53. Bauer PV, et al. Lactobacillus gasseri in the upper small intestine impacts an ACSL3-dependent fatty acid-sensing pathway regulating whole-body glucose homeostasis. *Cell Metab*. 2018;27(3):572-587.
54. Hagege H, et al. Quantitative analysis of chromosome conformation capture assays (3C-qPCR). *Nat Protoc*. 2007;2(7):1722-1733.